



HAL
open science

Oxidation of ethidium-based probes by biological radicals: mechanism, kinetics and implications for the detection of superoxide

Radoslaw Michalski, David Thiebaut, Bartosz Michalowski, Mehmet M Ayhan, Micael Hardy, Olivier Ouari, Michal Rostkowski, Renata Smulik-Izydorzcyk, Angelika Artelska, Andrzej Marcinek, et al.

► To cite this version:

Radoslaw Michalski, David Thiebaut, Bartosz Michalowski, Mehmet M Ayhan, Micael Hardy, et al.. Oxidation of ethidium-based probes by biological radicals: mechanism, kinetics and implications for the detection of superoxide. *Scientific Reports*, 2020, 10, 10.1038/s41598-020-75373-2 . hal-03244541

HAL Id: hal-03244541

<https://amu.hal.science/hal-03244541>

Submitted on 1 Jun 2021

HAL is a multi-disciplinary open access archive for the deposit and dissemination of scientific research documents, whether they are published or not. The documents may come from teaching and research institutions in France or abroad, or from public or private research centers.

L'archive ouverte pluridisciplinaire **HAL**, est destinée au dépôt et à la diffusion de documents scientifiques de niveau recherche, publiés ou non, émanant des établissements d'enseignement et de recherche français ou étrangers, des laboratoires publics ou privés.



Distributed under a Creative Commons Attribution 4.0 International License



OPEN

Oxidation of ethidium-based probes by biological radicals: mechanism, kinetics and implications for the detection of superoxide

Radosław Michalski^{1✉}, David Thiebaut², Bartosz Michałowski¹, Mehmet M. Ayhan³, Micael Hardy², Olivier Ouari², Michał Rostkowski¹, Renata Smulik-Izydorczyk¹, Angelika Artelska¹, Andrzej Marcinek¹, Jacek Zielonka⁴, Balaraman Kalyanaraman⁴ & Adam Sikora^{1✉}

Hydroethidine (HE) and hydropropidine (HPr⁺) are fluorogenic probes used for the detection of the intra- and extracellular superoxide radical anion (O₂^{•-}). In this study, we provide evidence that HE and HPr⁺ react rapidly with the biologically relevant radicals, including the hydroxyl radical, peroxy radicals, the trioxidocarbonate radical anion, nitrogen dioxide, and the glutathionyl radical, via one-electron oxidation, forming the corresponding radical cations. At physiological pH, the radical cations of the probes react rapidly with O₂^{•-}, leading to the specific 2-hydroxylated cationic products. We determined the rate constants of the reaction between O₂^{•-} and the radical cations of the probes. We also synthesized N-methylated analogs of HPr⁺ and HE which were used in mechanistic studies. Methylation of the amine groups was not found to prevent the reaction between the radical cation of the probe and the superoxide, but it significantly increased the lifetime of the radical cation and had a substantial effect on the profiles of the oxidation products by inhibiting the formation of dimeric products. We conclude that the N-methylated analogs of HE and HPr⁺ may be used as a scaffold for the design of a new generation of probes for intra- and extracellular superoxide.

The superoxide radical anion (O₂^{•-}) is the primary reactive oxygen species (ROS) produced *in vivo*. It is formed in the process of one-electron reduction of molecular oxygen, mediated by enzymes such as NAD(P)H oxidases¹ and xanthine oxidase². It is also produced in mitochondria, e.g., by the electron transport chain³. The superoxide radical anion itself is not highly reactive toward most biomolecules, but it can serve as a precursor of biologically relevant oxidants, such as hydrogen peroxide (H₂O₂) and peroxynitrite (ONOO⁻), initiating a cellular cascade of various oxidizing, nitrating and halogenating species^{4–7}.

When reactive oxygen and nitrogen species (ROS and RNS) are produced in cells in amounts sufficient to overcome the antioxidant defense, a state of “oxidative stress” occurs⁸. Oxidative stress has been linked to several pathophysiological states, including cancer, inflammation, reperfusion injuries, and aging^{9–11}. Therefore, it is essential to develop reliable probes and methods allowing for rigorous and accurate detection and characterization of ROS and RNS in biological samples. Among other approaches, fluorescent probes are used widely for ROS/RNS measurements, due mostly to their variety and versatility, as well as owing to the sensitivity of fluorescence-based techniques¹².

Of the fluorescent probes used for O₂^{•-} detection^{13–20}, hydroethidine (HE) has been found to be one of the most promising candidates. It has been applied in a variety of *in vitro* and *in vivo* systems, ranging from intracellular organelles to whole organs in live animals^{21–26}. The triphenylphosphonium-linked derivative of HE, known as Mito-HE (or MitoSOX Red), has been synthesized in order to detect O₂^{•-} produced in mitochondria²⁴.

¹Institute of Applied Radiation Chemistry, Lodz University of Technology, 90-924 Lodz, Poland. ²Aix Marseille Univ, CNRS, ICR, UMR 7273, 13013 Marseille, France. ³Department of Chemistry, Gebze Technical University, 41400, Gebze, Kocaeli, Turkey. ⁴Department of Biophysics and Free Radical Research Center, Medical College of Wisconsin, Milwaukee, WI 53226, USA. ✉email: radoslaw.michalski@p.lodz.pl; adam.sikora@p.lodz.pl

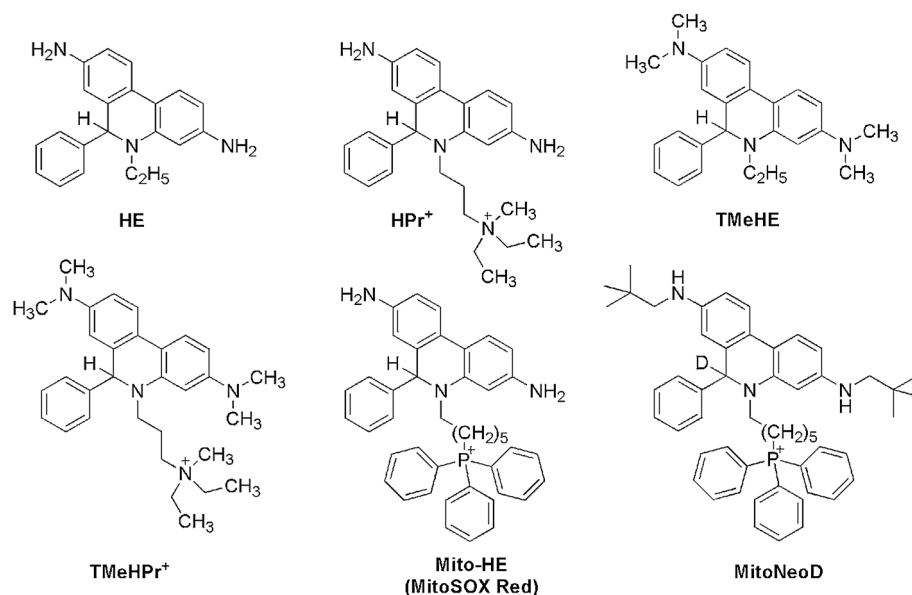


Figure 1. Chemical structures of hydroethidine (HE), hydropropidine (HPr⁺), N,N,N',N'-tetramethylhydroethidine (TMeHE), N,N,N',N'-tetramethylhydropropidine (TMeHPr⁺), mitochondria-targeted hydroethidine (Mito-HE), and mitochondria-targeted superoxide probe (MitoNeoD).

Another derivative of HE used to detect O₂^{•−} in isolated mitochondria and mouse heart mitochondria *in vivo* is MitoNeoD²⁷. A cell membrane-impermeable analog of HE, hydropropidine (HPr⁺), designed for the detection of extracellular O₂^{•−}²⁸, was used successfully to identify Nox2 inhibitors by monitoring O₂^{•−} production from activated NADPH oxidase directly by fluorescence in high-throughput screening assays^{29,30}. Although HE, Mito-HE, MitoNeoD, and HPr⁺, differ in their exact chemical structures (Fig. 1) and physicochemical properties, resulting in different subcellular distributions, their overall chemical reactivity is very similar^{24,27,28,31}.

The chemical reactivity of HE-based probes has been studied in some detail^{28,31–37}, including their reaction kinetics and reactivity toward various one- and two-electron oxidants. The main and unequivocal advantage of using hydroethidine-based probes is the specific formation of 2-hydroxylated products in the reaction with O₂^{•−}, which are unique markers of superoxide production. The most extensively studied hydroethidine-based probe is HE, and a large amount of data are available concerning its reactivity, including its stoichiometry and oxidation mechanism^{36,38,39}. According to the literature, in the presence of varying fluxes of O₂^{•−} the only SOD-sensitive product formed from the reaction between HE and O₂^{•−} is 2-OH-E⁺³⁹. Irrespective of the one-electron oxidant present, the first step in the oxidation reaction of HE leads to the formation of an intermediate that is thought to be either a radical cation or an aromatic aminyl radical, which in the presence of O₂^{•−} is subsequently converted into 2-OH-E⁺. In the absence of the superoxide, one-electron oxidation of HE results in the formation of E⁺ and characteristic dimeric products, such as HE-HE, HE-E⁺, and E⁺-E⁺, the distribution of which depends on the reaction conditions (Fig. 2). The same has been shown to be true for the HPr⁺ probe²⁸. Although much work has focused on elucidating the oxidation mechanism of HE-based probes, more comprehensive knowledge of their chemical reactivity toward biologically relevant oxidants is needed for their reliable use in biological systems and for accurate interpretation of experimental data.

Here, we present a detailed mechanistic study of the one-electron oxidation of hydropropidine, a water-soluble analogue of HE. We report the kinetics of reactions between HPr⁺ and the biologically relevant oxidants, such as glutathionyl radical (GS[•]), nitrogen dioxide (•NO₂), and trioxidocarbonate radical anion (CO₃^{•−}), as well as the kinetics of the reaction of the probe-derived radical cation (HPr^{•2+}) with O₂^{•−}. The results are complemented by spectroscopic characterization of the one-electron oxidation products of HPr⁺ and HE in cryogenic matrices, along with quantum mechanical calculations. The mechanistic conclusions are supported by detailed analyses of the oxidation products. We also introduce novel N-methylated HE and HPr⁺ derivatives (Fig. 1), N,N,N',N'-tetramethylhydroethidine (TMeHE) and N,N,N',N'-tetramethylhydropropidine (TMeHPr⁺), both for mechanistic studies and as a chemical scaffold for the development of new HE-based probes for O₂^{•−}.

Results

Kinetic studies using pulse radiolysis. *Reaction of HPr⁺ and HE with •NO₂ and CO₃^{•−}.* Decomposition of peroxyntirite in the presence of CO₂ leads to the formation of •NO₂ and CO₃^{•−}⁴. To study the reaction of •NO₂ with the HPr⁺ probe, •NO₂ was generated by pulse radiolysis of an aqueous solution of HPr⁺, as described in detail in the Supplementary Information (SI). The reaction of •NO₂ and HPr⁺ led to the formation of a product with two characteristic absorption bands: a narrow band located at 460 nm and a broad band with a maximum at 720 nm (Fig. 3A). Similar absorption bands were observed during the reaction of •NO₂ with HE instead of HPr⁺ (Fig. 3B). The second-order rate constants determined for the reaction of •NO₂ with HPr⁺ and HE are equal to $(6.5 \pm 0.3) \times 10^8 \text{ M}^{-1}\text{s}^{-1}$ and $(6.8 \pm 0.3) \times 10^8 \text{ M}^{-1}\text{s}^{-1}$, respectively (Supplementary Table S1

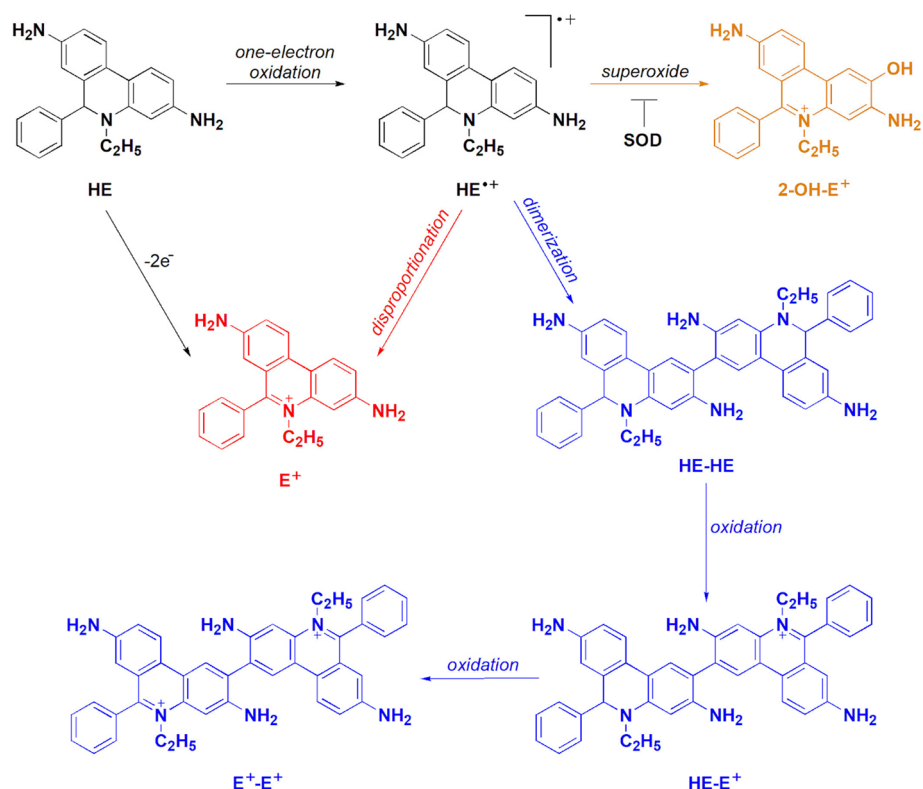


Figure 2. Oxidative chemistry of the HE probe.

and Fig. S1). We have also carried out the kinetic simulations for the reaction of HPr^+ with both oxidants that support the experimental data. The used kinetic models are presented in the SI.

The oxidation of HPr^+ and HE by $\text{CO}_3^{\bullet-}$ was also studied. The reaction of both probes with $\text{CO}_3^{\bullet-}$ was performed at pH 10.3 to ensure the fast and complete conversion of the hydroxyl radical produced during radiolysis into $\text{CO}_3^{\bullet-}$ (see SI). Initially, after the electron pulse, a broad weak absorption band around 600 nm appeared (Fig. 3C,D), consistent with the formation of $\text{CO}_3^{\bullet-}$ ⁴⁰. Over the course of the reaction, this absorption band was replaced by the absorption bands of the oxidation product of HPr^+ (Fig. 3C) when the solute was HPr^+ or by the bands for the oxidation product of HE (Fig. 3D) when HE was present in the reaction mixture. Both HPr^+ and HE were oxidized by $\text{CO}_3^{\bullet-}$ at pH 10.3. The second-order rate constants are equal to $(4.8 \pm 0.6) \times 10^9 \text{ M}^{-1} \text{ s}^{-1}$ and $(4.6 \pm 0.2) \times 10^9 \text{ M}^{-1} \text{ s}^{-1}$, respectively (Supplementary Table S1 and Fig. S1). We have also performed the kinetic simulations for the reaction of HPr^+ with N_3^{\bullet} and the data are available in SI.

Oxidation of HPr^+ and HE by N_3^{\bullet} at different pH. To confirm that both $\bullet\text{NO}_2$ and $\text{CO}_3^{\bullet-}$ react with the probes *via* one-electron transfer, we performed additional studies at two different pH values using the azidyl (N_3^{\bullet}) radical as a strong, but selective one-electron oxidant. The transient absorption spectra obtained from the reaction of HPr^+ with the N_3^{\bullet} radical at pH 7.4 and pH 10.5 are presented in Fig. 3E. The same spectrum was recorded for both pH values, with strong absorption observed around 460 nm and an additional broad band of lower intensity with its maximum observed at 720 nm. The second-order rate constant of the reaction between HPr^+ and N_3^{\bullet} , $k = (4.8 \pm 0.2) \times 10^9 \text{ M}^{-1} \text{ s}^{-1}$ (Supplementary Table S1 and Fig. S1), was determined from the dependence of the kinetics of the increase in absorption at 460 nm on the HPr^+ concentration. Figure 3F shows the absorption spectra of the transient species formed during the reaction of N_3^{\bullet} with HE at pH 7.4 and pH 10.5. Similar to the case of HPr^+ , the same species was observed at both pH values. The determined rate constant for the reaction of the N_3^{\bullet} radical with HE, at pH 7.4 is equal to $(4.2 \pm 0.3) \times 10^9 \text{ M}^{-1} \text{ s}^{-1}$ (Supplementary Table S1 and Fig. S1).

Oxidation of HPr^+ and HE by HO^{\bullet} and $\text{Br}_2^{\bullet-}$. We used the hydroxyl radical (HO^{\bullet}) and the dibromide radical anion ($\text{Br}_2^{\bullet-}$) to better characterize the reactivity of the studied probes toward one-electron oxidants. Pulse radiolytic generation of the HO^{\bullet} and $\text{Br}_2^{\bullet-}$ radicals in the presence of HPr^+ led to the appearance of characteristic spectra observed previously during the reaction of the probe with $\bullet\text{NO}_2$, $\text{CO}_3^{\bullet-}$, and N_3^{\bullet} oxidants (Fig. 3A,C,E). The hydroxyl radical is known to be a non-selective oxidant that reacts with aromatic compounds by electron transfer, hydrogen atom abstraction, and/or addition to the double bond. Due to the similarity of the observed spectrum for HO^{\bullet} -induced oxidation product to the other spectra obtained with selective one-electron oxidants, it is reasonable to assume that the HPr^+ probe reacts with HO^{\bullet} primarily *via* electron transfer. This has been previously reported for HE³⁵.

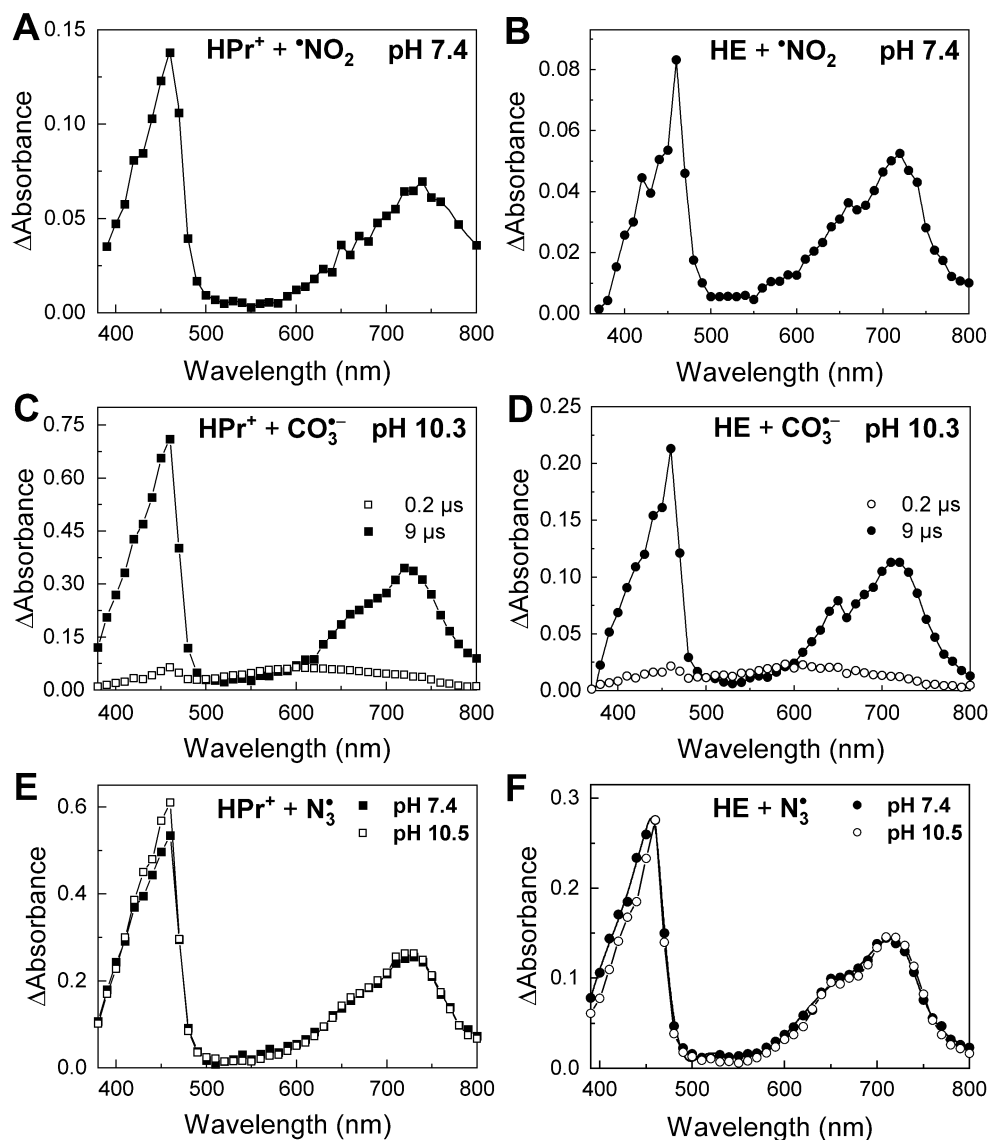


Figure 3. Absorption spectra of one-electron oxidation products of HPr⁺ and HE. (A) Transient absorption spectrum recorded after pulse radiolysis of N₂-saturated solutions of 0.1 M NaNO₃, 1 M *t*-BuOH, and 50 mM phosphate buffer at pH 7.4 containing 50 μM HPr⁺ recorded 25 μs after the electron pulse. Radiation dose: 62 Gy. (B) same as (A) but the solution contained 75 μM HE. Radiation dose: 50 Gy. (C) Transient absorption spectra obtained by pulse radiolysis of 50 μM HPr⁺ in N₂O-saturated aqueous solution containing 0.25 M Na₂CO₃ and 0.25 M NaHCO₃ (pH 10.3). Spectra recorded (open squares) 0.2 μs and (solid squares) 9 μs after the electron pulse. Radiation dose: 53 Gy. (D) same as (C) but the solution contained 100 μM HE instead of HPr⁺ and 10% vol. CH₃CN. Spectra recorded (open circles) 0.2 μs and (solid circles) 9 μs after the electron pulse. Radiation dose 52 Gy. (E) Transient absorption spectra recorded after pulse radiolysis of HPr⁺ (50 μM) in N₂O-saturated solution containing phosphate buffer (50 mM) with NaN₃ (0.1 M). Spectra recorded (solid squares) at pH 7.4, radiation dose 54 Gy and (open squares) at pH 10.5, radiation dose 54 Gy (the solution was adjusted with 0.1 M NaOH to pH 10.5). (F) same as (E) but the solution contained HE instead of HPr⁺ and 10% CH₃CN (solid circles—75 μM HE, pH 7.4, radiation dose 65 Gy; open circles—100 μM HE, pH 10.5, radiation dose 63 Gy). All samples were 1 cm thick.

The rate constants for the reactions of HO[•] and Br₂^{•-} with HPr⁺ were found to be equal to $(1.2 \pm 0.1) \times 10^{10} \text{ M}^{-1} \text{ s}^{-1}$ and $(3.9 \pm 0.2) \times 10^9 \text{ M}^{-1} \text{ s}^{-1}$, respectively (Supplementary Table S1).

In the case of HE, we were unable to determine the appropriate rate constant with HO[•], due to its side reactions with acetonitrile, which was used to improve the solubility of the probe in aqueous solution. The rate constant for the reactions of HE with Br₂^{•-} was found to be equal to $(3.7 \pm 0.1) \times 10^9 \text{ M}^{-1} \text{ s}^{-1}$ (Supplementary Table S1).

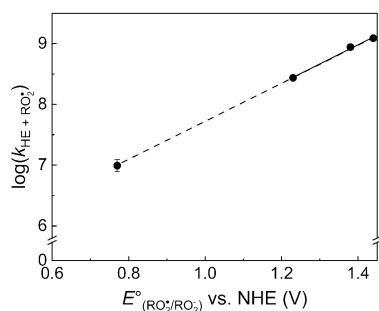


Figure 4. Relationship between the decimal logarithm of the second-order rate constants [$\log(k_{\text{HE}} + \text{ROO}^\bullet)$] and the standard electrode potentials of peroxy radicals [$E^\circ(\text{ROO}^\bullet/\text{ROO}^-)$], the kinetic and thermodynamic parameters of the reaction between HE and selected peroxy radicals. The dashed line shows the extrapolation of the relationship to the value of the standard electrode potential of HO_2^\bullet (0.77 V). The standard electrode potential of the $\text{HO}_2^\bullet/\text{HO}_2^-$ couple was calculated using the pKa value of hydrogen peroxide (11.7), the standard electrode potential of the $\text{HO}_2^\bullet, \text{H}^+/\text{H}_2\text{O}_2$ couple (1.46 V)⁴⁹, and 1 M concentration of H^+ (pH 0), according to the standard state conditions⁴⁹. The standard electrode potentials were taken from the literature⁷¹.

Reaction of GS^\bullet and CysS^\bullet with HPr^+ and HE. Under conditions of oxidative stress, initial scavenging of free radicals by reduced glutathione or cysteine leads to the formation of the thiyl radical, which reactivity towards the redox probes should also be considered. Therefore, we generated the biologically relevant thiyl radicals from glutathione and cysteine, abbreviated as GS^\bullet and CysS^\bullet , respectively, to monitor their reaction with the HPr^+ and HE probes. One should note that GS^\bullet and CysS^\bullet exist in equilibrium with their carbon-centered radicals as reported by Schöneich and coworkers⁴¹. Although this equilibrium is shifted to the side of the sulfur-centered radicals and is rather fast⁴², it may affect the reaction kinetics, and thus the determined rate constants should be treated as the “apparent” values.

In the presence of HPr^+ or HE, the build-up of the absorption bands characteristic for their radical cations was completed within 30 μs after pulse irradiation (Supplementary Fig. S2). The second-order rate constants of the GS^\bullet reaction with HPr^+ or HE at pH 7.4 were found to be $(3.8 \pm 0.3) \times 10^8 \text{ M}^{-1}\text{s}^{-1}$ and $(2.9 \pm 0.1) \times 10^8 \text{ M}^{-1}\text{s}^{-1}$, respectively (Supplementary Fig. S2 and Table S1). The second-order rate constants of the CysS^\bullet radical reactions with both probes have been determined to be equal to $(2.4 \pm 0.1) \times 10^8 \text{ M}^{-1}\text{s}^{-1}$ for HPr^+ and $(4.3 \pm 0.2) \times 10^8 \text{ M}^{-1}\text{s}^{-1}$ for HE (Supplementary Fig. S2 and Table S1).

Reactivity of HE toward peroxy radicals. Peroxy-type radicals are another class of strong one-electron oxidants of biological relevance. We used a series of pulse-generated model peroxy radicals to study the reactivity of HE towards these oxidants. The chloromethylperoxy radical reacted with HE to produce a transient species possessing the characteristic absorption spectra observed in the reaction of HE with the other used oxidants (Supplementary Fig. S3). The second-order rate constants determined at pH 7.4 for the reaction of HE with $\text{CCl}_3\text{OO}^\bullet$, $\text{CHCl}_2\text{OO}^\bullet$, and $\text{CH}_2\text{ClOO}^\bullet$ radicals are equal to $(1.23 \pm 0.02) \times 10^9$, $(8.8 \pm 0.1) \times 10^8$, and $(2.7 \pm 0.1) \times 10^8 \text{ M}^{-1}\text{s}^{-1}$, respectively (Fig. 4 and Supplementary Table S2). This indicates that the rate constant of the reaction can be correlated with the strength (standard electrode potential) of the oxidant. Extrapolating the dependence of $\log k$ on the standard standard electrode potentials of the oxidants to the value calculated for the hydridodioxigen($^\bullet$) (HO_2^\bullet , also known as the hydroperoxyl radical), enabled us to estimate the rate constant for the reaction of this oxidant with HE ($\sim 1 \times 10^7 \text{ M}^{-1}\text{s}^{-1}$, Fig. 4 and Supplementary Table S2).

Low-temperature radiolysis and quantum-mechanical calculations. Due to its inhibitory effect on recombination and fragmentation processes, a rigid frozen matrix allows for direct observation of the primary oxidation products of solute molecules, such as radical cations. Therefore, additional experiments were performed to ensure correct identification of the transients observed in the pulse radiolysis experiments at room temperature. Upon irradiation of a frozen solution of HPr^+ in a mixture of 1-butyl-3-methylimidazolium hexafluorophosphate and methylene chloride ($\text{BMIM}^+\text{PF}_6^- : \text{CH}_2\text{Cl}_2$, 1:1, v/v) at 77 K, a UV–Vis absorption spectrum was recorded with a strong absorption band located around 460 nm and minor absorption bands at 678 and 748 nm. This spectrum was provisionally assigned to the radical cation of HPr^+ ($\text{HPr}^{\bullet 2+}$) (Fig. 5A). Irradiation of HE embedded in the frozen mixture of $\text{BMIM}^+\text{PF}_6^- : \text{CH}_2\text{Cl}_2$ led to the formation of a species possessing the same absorption band profile, and this product was ascribed to the radical cation of HE ($\text{HE}^{\bullet +}$) (Fig. 5B).

To further confirm this assignment and exclude the possibility of rapid deprotonation of the radical cations formed during irradiation of the cryogenic matrices, we also performed spectroscopic characterization of the radical cations of methylethidine (MeE) and TMeHE in the low-temperature matrices. MeE bears a methyl group in position 6, in the place of a hydrogen atom in HE. In contrast to HE, the formation of an ethidium cation is not possible following one-electron oxidation. The species formed upon irradiation of the frozen solution of MeE in a $\text{BMIM}^+\text{PF}_6^- : \text{CH}_2\text{Cl}_2$ mixture (1:1, v/v) at 77 K, was characterized by a UV–Vis spectrum with a strong absorption band located around 460 nm and minor absorption bands at 670 nm and 740 nm. This spectrum was assigned to the radical cation of MeE ($\text{MeE}^{\bullet +}$) (Fig. 5C). To test the possibility of deprotonation of the radical

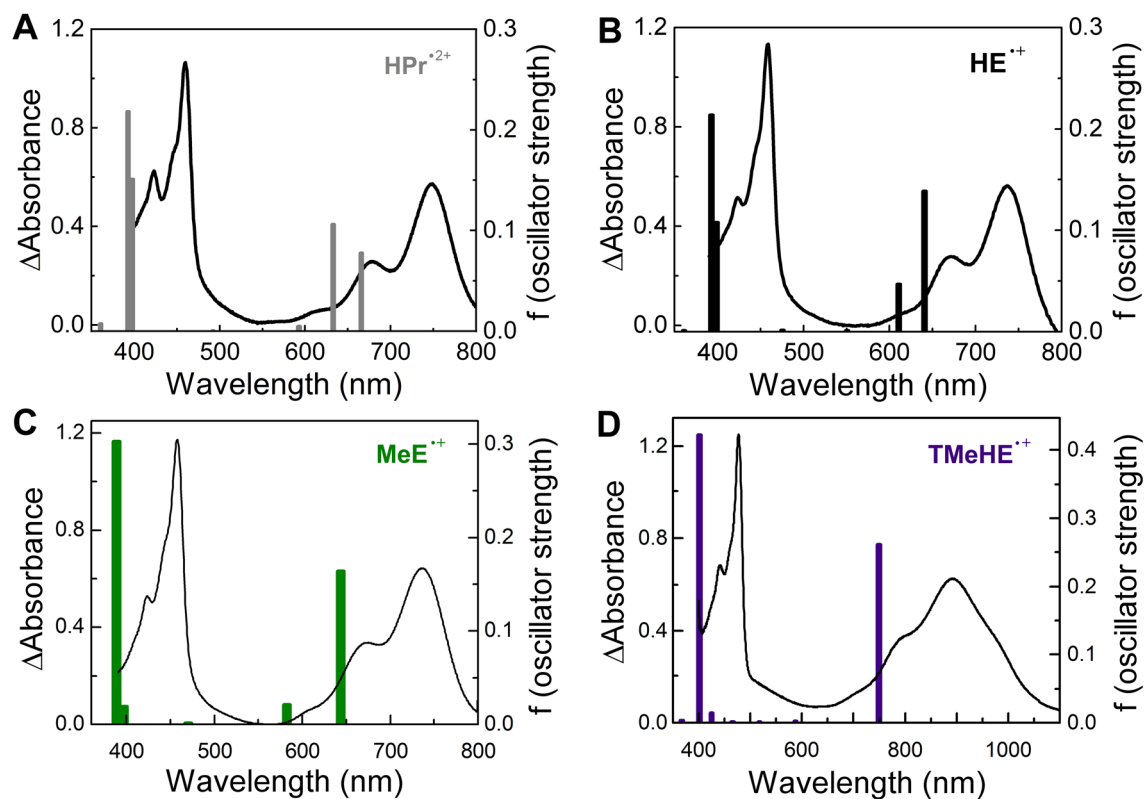


Figure 5. Comparison between the experimental and calculated spectra of the one-electron oxidation products of HPr⁺, HE, MeE, and TMeHE. (A–D, respectively). Electronic absorption spectra obtained by radiolysis of HPr⁺ (2 mM), HE (8.6 mM), MeE (10 mM), and TMeHE (10 mM), respectively, embedded in low temperature glass of BMIM⁺PF₆⁻ : CH₂Cl₂ (1:1, v/v) at 77 K. (the sample of HPr⁺ received a radiation dose of 5.8 kGy, HE received a radiation dose of 27 kGy, the samples of MeE and TMeHE received a radiation dose of 36 kGy, all samples were ~ 1 mm thick.) Excitation energies of HPr^{•2+}, HE^{•+}, MeE^{•+}, and TMeHE^{•+} obtained from TD-DFT quantum mechanical calculations are shown as vertical bars.

cation from the exocyclic amine groups, analogous experiments were performed for TMeHE (Fig. 5D). For MeE and TMeHE, similar electronic absorption spectra to those obtained upon oxidation of HPr⁺ and HE were recorded. Interestingly, for the radical cation of TMeHE (TMeHE^{•+}) the long-wavelength absorption band was red-shifted compared to those for HPr^{•2+}, HE^{•+} and MeE^{•+}.

The results of cryogenic measurements were complemented by quantum mechanical calculations of electron spin densities and excited-state transitions. The density functional theory (DFT) calculations for the radical cations of HPr⁺, HE, and their analogs were performed at the B3LYP/6-311+G(d,p) level. The geometry and electronic structures of the radical cations were calculated and the absorption spectra of the species were computed. The results are reported in Fig. 5 and Supplementary Fig. S4, and compared with the experimental data from radiolysis of frozen glasses in Supplementary Table S3. The results of TD-DFT calculations for HPr^{•2+}, HE^{•+}, MeE^{•+}, and TMeHE^{•+} are in reasonable agreement with the experimental data obtained from cryogenic measurements (Fig. 5). The shifts of the absorption bands (~0.25–0.5 eV) are typical for these types of calculations and for the B3LYP functional⁴³, and can also be partially attributed to the solvent effect, as the calculations were performed *in vacuo*. Moreover, the ratios of the intensities of the two absorption bands in the experimental spectra and of the calculated transitions remain in agreement. It should also be noted, that the red shift for the long-wavelength absorption band of TMeHE^{•+} is in agreement with TD-DFT-based predictions of the effect of methylation of the –NH₂ groups on the electronic transitions in the radical cation. Thus, the spectra obtained from TD-DFT calculations are in agreement with the assignment of the species observed in radiolytic studies to the radical cations of HE, HPr⁺, MeE, and TMeHE.

Analysis of the Mulliken atomic spin densities of the HPr⁺ and HE radical cations reveals that the highest spin density is located at the C-2 and C-12 carbon atoms (Supplementary Fig. S4 and Table S3). Similar spin distributions were calculated for the radical cations of MeE and TMeHE (Supplementary Fig. S4 and Table S3).

Stabilization of the probe radical cation by methylation of the amine groups. One-electron oxidation of HE and HPr⁺ is known to result in the formation of dimeric products, with two phenanthridine moieties forming a covalent 2,2' carbon-carbon bond^{28,31}. We anticipated that methylation of the amine groups adjacent to the C-2 carbon atoms would result in significant steric hindrance for a dimerization reaction, while still allowing a reaction with O₂^{•-}, thereby simplifying the profiles of the oxidation products of the probes. In order to test the effect of methylation of the amine groups on the reactivity of the radical cations produced, we

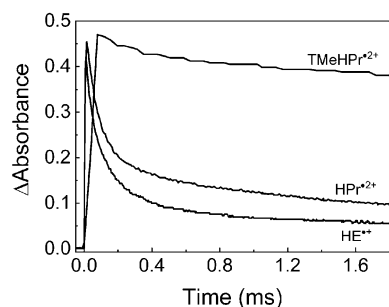


Figure 6. Decay kinetics of radical cations of HE, HPr⁺, and TMeHPr⁺. The decays were monitored at 460 nm for HE^{•+} and HPr^{•2+}, and at 480 nm for TMeHPr^{•2+}. Radical cations were generated by the irradiation of solutions containing 0.1 M of NaN₃, 50 mM of phosphate buffer (pH 7.4), and 100 μM of HE, or 100 μM of HPr⁺, or 60 μM of TMeHPr⁺. Radiation doses: 59 Gy for HE, 55 Gy for HPr⁺, and 62 Gy for TMeHPr⁺. Optical path-length: 1 cm.

compared the rates of HPr^{•2+} and HE^{•+} decay with the rate of TMeHPr^{•2+} decay, as well as the rates of the reactions of HPr^{•2+} and TMeHPr^{•2+} with O₂^{•-}. Due to limited water solubility, in the case of TMeHE, we were unable to obtain the sufficient concentration for pulse radiolysis experiments.

The kinetic traces for the decay of HE^{•+}, HPr^{•2+} and TMeHPr^{•2+} are presented in Fig. 6. Using the evaluated molar absorption coefficient of HPr^{•2+} ($\epsilon_{460\text{nm}} = 3.0 \times 10^4 \text{ M}^{-1}\text{cm}^{-1}$, Supplementary Table S4) and HE^{•+} ($\epsilon_{460\text{nm}} = 1.7 \times 10^4 \text{ M}^{-1}\text{cm}^{-1}$, Supplementary Table S4), the rate constants for the observed second-order decay of HPr^{•2+} and HE^{•+} were estimated to be equal to $(3.3 \pm 0.1) \times 10^8 \text{ M}^{-1}\text{s}^{-1}$ and $(2.7 \pm 0.2) \times 10^8 \text{ M}^{-1}\text{s}^{-1}$, respectively (Table S4). The rate constant of TMeHPr^{•2+} was not determined, because TMeHPr^{•2+} decay is complex and does not follow simple bimolecular decay kinetics. However, TMeHPr^{•2+} was significantly more stable than HE^{•+} or HPr^{•2+} (Fig. 6), demonstrating that N-methylation leads to the increased lifetime of the radical cation.

Reaction of the radical cation of the probe with O₂^{•-}. We used TMeHPr⁺ to demonstrate the reaction of the radical cation of the probe with O₂^{•-} and to determine its rate constant. We anticipated that the rate of this reaction would not be significantly affected by the N-methylation of amine groups, and thus it should be characteristic for all HE analogues. The much slower decay of TMeHPr^{•2+} than HPr^{•2+} and HE^{•+} (Fig. 6) enabled more accurate determination of the rate constant.

To monitor the reaction of the radical cation TMeHPr^{•2+} with O₂^{•-}, both species were generated simultaneously by pulse radiolysis, as described in the SI. One-electron oxidation of TMeHPr⁺ led to the formation of TMeHPr^{•2+} (Fig. 7A), the lifetime of which was significantly shortened in the presence of O₂^{•-} (Fig. 7B). This directly demonstrates for the first time the reaction of the probe radical cation with O₂^{•-}. The rate constant of the reaction between the generated radical cation and O₂^{•-} was determined by monitoring the decay of the radical cation of TMeHPr⁺ at 480 nm with different radiation doses to modulate the concentration of O₂^{•-} (see SI). The second-order rate constant determined from the dependence of the observed rate constant on the initial O₂^{•-} concentration (Fig. 7C) is equal to $(5.0 \pm 0.1) \times 10^8 \text{ M}^{-1}\text{s}^{-1}$ (Supplementary Table S4). The second-order rate constant for the reaction of HPr^{•2+} with O₂^{•-} was also determined under analogous experimental conditions, and is equal to $(7.4 \pm 0.1) \times 10^8 \text{ M}^{-1}\text{s}^{-1}$ (Supplementary Table S4 and Fig. S5). At the concentrations of superoxide generated in these experiments, the self-decay of superoxide *via* dismutation reaction occurs over a significantly longer timescale, and therefore its effect on the observed kinetics can be neglected. We attribute a small, but non-zero intercept observed in Fig. 7C to the self-decay of TMeHPr^{•2+} in the absence of O₂^{•-}.

Characterization of the stable products of one-electron oxidation of TMeHE and TMeHPr⁺. We have demonstrated that N-methylation of the probes increases the lifetime of the radical cation (Fig. 6), which may be due to the hindered dimerization process. To determine the products of one-electron oxidation of the methylated probes, we performed titration of a set of TMeHPr⁺ samples, with different concentrations of potassium ferricyanide as a one-electron oxidant. In our previous studies, we found ferricyanide oxidizes HE and HPr⁺ to form E⁺ and Pr⁺⁺, respectively, as well as dimeric products^{28,31}. The UPLC traces obtained in the present study for the incubation mixtures containing TMeHPr⁺ and various concentration of Fe(CN)₆³⁻ are presented in Fig. 8A. The sole product observed for this reaction is TMePr⁺⁺, which was eluted at 1.45 min (Fig. 8A). These data are in agreement with the UV-Vis measurements conducted under the same experimental conditions (Fig. 8B). The absorption band of TMePr⁺⁺ peaking at 547 nm, which was identified on the basis of the absorption spectrum of its original standard, increases linearly with the addition of Fe(CN)₆³⁻ (Fig. 8B, upper inset). The addition of Fe(CN)₆³⁻ at a concentration higher than 100 μM to the solution containing TMeHPr⁺ at a concentration of 50 μM did not cause further increases in TMePr⁺⁺, suggesting a 1:2 stoichiometry. The changes observed for the absorption maximum of K₃Fe(CN)₆ at 420 nm are also shown in Fig. 8B. It can be calculated that the concentration of the remaining K₃Fe(CN)₆ is equal to 100 μM for the mixture of 50 μM of TMeHPr⁺ and 200 μM of K₃Fe(CN)₆ ($\epsilon_{240\text{nm}} = 1023 \text{ M}^{-1}\text{cm}^{-1}$)⁴⁴. For the purpose of comparison, the absorption spectrum of a 1 mM solution of K₃Fe(CN)₆ is also shown in Fig. 8B marked by a black dashed line. All presented data indicate 1:2

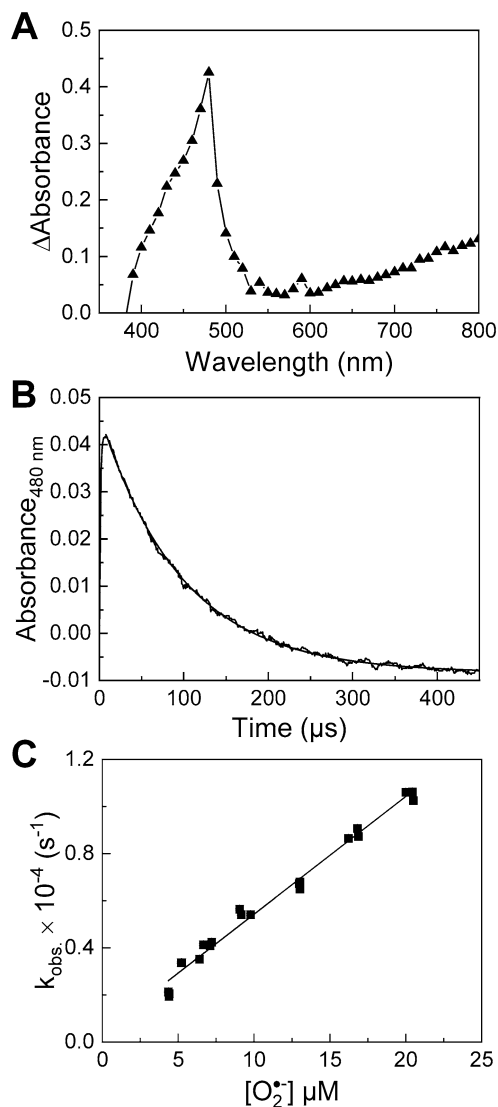


Figure 7. Reaction of TMeHPr \bullet^{2+} with superoxide. (A) Transient absorption spectrum recorded after pulse radiolysis of TMeHPr $^{+}$ (50 μM) in an N_2O -saturated solution containing phosphate buffer (50 mM, pH 7.4) with NaN_3 (0.1 M). The sample was 1 cm thick, radiation dose: 55 Gy. The spectrum was recorded 9 μs after the electron pulse. (B) Decay of TMeHPr \bullet^{2+} due to the reaction with $\text{O}_2^{\bullet-}$ monitored at 480 nm. The kinetic trace was recorded after pulse radiolysis of an oxygen-saturated aqueous solution containing TMeHPr $^{+}$ (180 μM), NaN_3 (3 mM), formate (50 mM), and phosphate buffer (5 mM, pH 7.4). Radiation dose: 39 Gy. The black lines show the kinetic trace and the pseudo-first order kinetics fit (k_{obs}) to the experimental data. The concentration of TMeHPr \bullet^{2+} was calculated using the previously determined extinction coefficient of $26,100 \text{ M}^{-1}\text{cm}^{-1}$. (C) Plot of k_{obs} against the initial concentration of $\text{O}_2^{\bullet-}$.

(HPr $^{+}$:Fe(CN) $_6^{3-}$) stoichiometry of the observed reaction and the absence of corresponding dimers formed by the N-methylated analog of HPr $^{+}$. Similar analyses were performed for TMeHE and compared to HE. Using LC/MS we detected TMeE $^{+}$ (the X-Ray structure is presented in SI) as the product, which was eluted at a retention time of 2.44 min (Supplementary Fig. S6). The small peak observed at 2.3 min (Supplementary Fig. S6) was identified as a trimethylethidium cation originating from residual amounts of trimethyl-hydroethidine detected in the TMeHE sample. In the case of HE (Supplementary Fig. S6), oxidation of the probe with the ferricyanide anion led to the formation of several products, the distribution of which was dependent on the concentration of the oxidant. In agreement with our previous results³¹, LC/MS analyses showed that, in addition to E $^{+}$, HE dimers are formed. In the case of TMeHE, no dimers were detected under the same conditions (Supplementary Fig. S6). All the presented data indicate that N-methylation of the probes blocks the dimerization process, leading to the formation of TMeE $^{+}$ or TMePr $^{++}$ as the sole products formed upon one-electron oxidation. In contrast, in the cases of HE and HPr $^{+}$ the dimeric products are formed upon one-electron oxidation, and the stoichiometry of their reaction with the

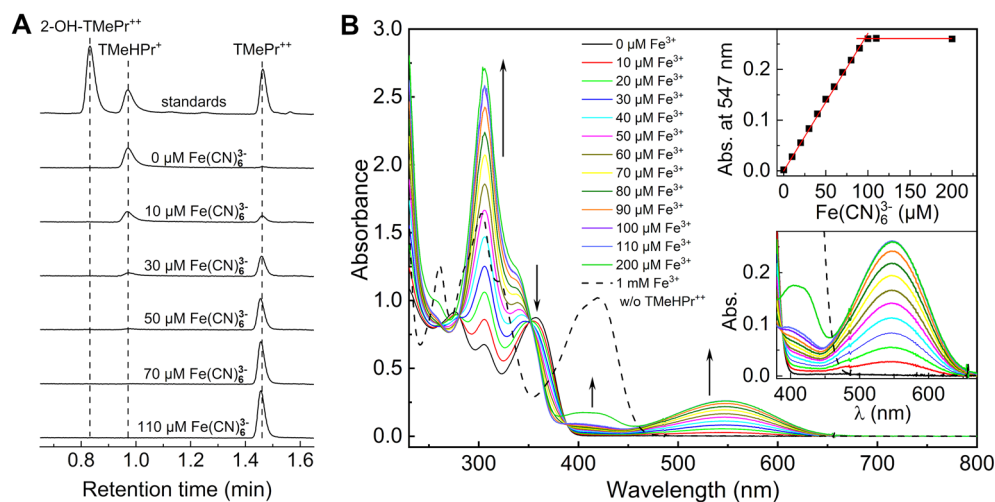


Figure 8. Oxidation of TMeHPr⁺ by the ferricyanide anion. **(A)** UPLC traces obtained for mixtures containing 50 μM TMeHPr⁺ and 0–110 μM ferricyanide anion. The concentration of the standards was 50 μM for TMeHPr⁺, 2-OH-TMePr⁺, and TMePr⁺. The analytical wavelength used for UV–Vis detection: $\lambda = 370 \pm 5$ nm. **(B)** UV–Vis absorption spectra of mixtures containing 50 μM TMeHPr⁺ and various concentrations of Fe(CN)₆³⁻ (0–200 μM, represented in the legend as Fe³⁺). Upper inset: dependence of absorbance at 547 nm on Fe(CN)₆³⁻ concentration. Lower inset: changes in absorbance between 400 and 670 nm.

ferricyanide anion is higher due to additional depletion of the oxidant during the formation of the fully oxidized dimers, E⁺-E⁺ and Pr⁺⁺-Pr⁺⁺²⁸.

Oxidation of TMeHE by O₂^{•-} in enzymatic and cellular systems. In order to evaluate the impact of methylation of the exocyclic amino groups of HE on its reactivity toward O₂^{•-}, we incubated TMeHE in a mixture of hypoxanthine and xanthine oxidase as a source of O₂^{•-}. In the reaction mixture, the chelating agent dtpa was used to avoid the interference with metal ions such as copper and/or iron that can accelerate the dismutation of O₂^{•-} or initiate oxidation of the probe *via* Fenton reaction.

The UPLC analyses revealed the build-up of a peak with a retention time of 1.73 min (Supplementary Fig. S7) corresponding to 2-OH-TMeE⁺. This was confirmed by comparison to the retention time of an independently synthesized standard of 2-OH-TMeE⁺ (Supplementary Fig. S7, X-Ray structure available in SI). The influence of SOD and catalase on the formation of 2-OH-TMeE⁺ was also determined (Supplementary Fig. S7). The SOD completely abolished the peak assigned to 2-OH-TMeE⁺. In turn, catalase increased the yield of 2-OH-TMeE⁺ production substantially, which we attribute to an increased steady-state concentration of TMeHE^{•+} ready to react with O₂^{•-} and produced by catalase in a peroxidase-like cycle. After three hours of incubation in the absence of XO and SOD, a small amount of 2-OH-TMeE⁺ was formed due to autoxidation of the probe in the presence of oxygen. Autoxidation has also been shown to occur in the case of HE probe but to a lesser extent³². The formation of other nonspecific oxidation products, such as the corresponding dimers, was not observed. These results indicate that methylation of the exocyclic amine groups of HE does not prevent the probe from trapping superoxide.

To determine whether the TMeHE probe is able to report intracellular superoxide, RAW 264.7 macrophages were stimulated with phorbol 12-myristate 13-acetate (PMA) in the presence of the TMeHE probe. Incubation of macrophages activated to produce O₂^{•-} in the presence of TMeHE resulted in the formation of 2-OH-TMeE⁺ (Fig. 9). A significant increase in the amount of 2-OH-TMeE⁺, but not of TMeE⁺, was detected upon stimulation of the cells with PMA (Fig. 9C).

Discussion

The presented results demonstrate that the peroxynitrite-derived radicals •NO₂ and CO₃^{•-}, as well as GS[•] and CysS[•], are capable of oxidizing HE and HPr⁺ probes *via* a single electron transfer pathway. The values of the determined rate constants are shown in Supplementary Table S1. Nonetheless, in the presence of glutathione and proteins at millimolar concentrations, the direct reaction of •NO₂ and CO₃^{•-} with HE or HPr⁺ seems rather unlikely under *in vivo* conditions. The alternate scenario is that the protein-centered radicals induced by •NO₂, CO₃^{•-}, and other strong one-electron oxidants may oxidize the probe and increase the yields of 2-OH-E⁺ observed *in vivo*. Recently, it also has been proposed that nitrosoperoxocarbonate, ONOOCO₂⁻, may be more stable than initially assumed and may also act as a strong one-electron oxidant⁴⁵. Prütz et al have shown that upon initial protein oxidation, intramolecular electron transfer leads to the formation of tyrosyl radicals (E[•](TyrO[•], H⁺/TyrOH) = 0.96 V)^{46,47}. In turn, intramolecular electron transfer from the tyrosyl radical to the cysteine residue leads to thiyl radicals (CysS[•])⁴⁸. The redox potentials of both couples (TyrO[•], H⁺/TyrOH and CysS[•], H⁺/CysSH) are similar and both types of radicals may be involved in HE oxidation *in vivo*⁴⁸. Because the radical cation of HE and its derivatives react rapidly with O₂^{•-} to form hydroxylated products, the presence of such oxidants may

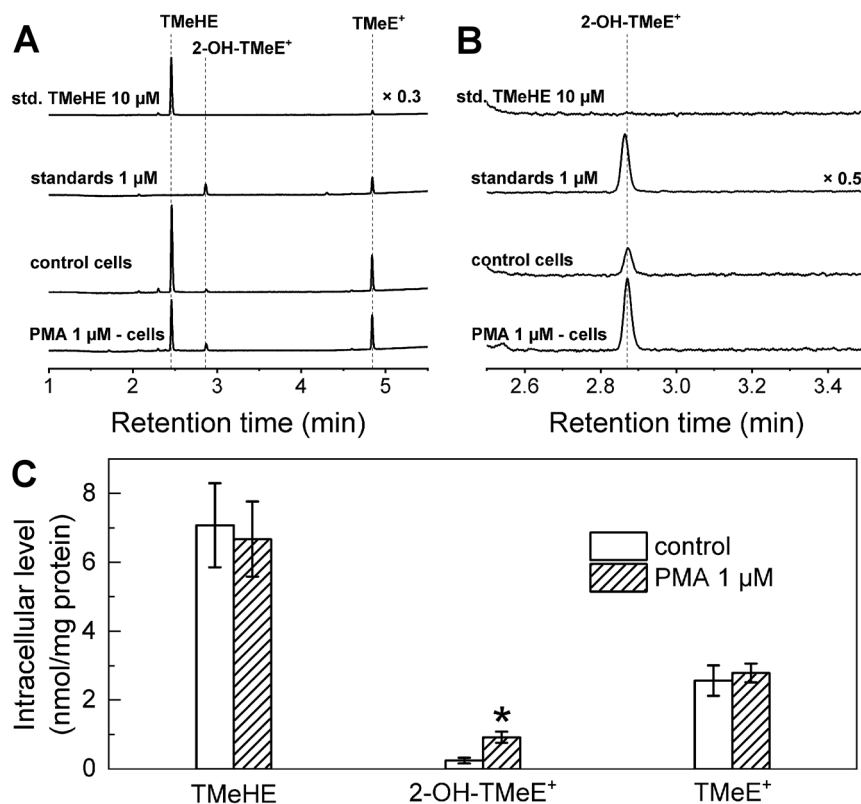


Figure 9. Detection of $O_2^{\bullet-}$ in RAW 264.7 cells stimulated PMA (1 μ M, 1 h), using TMeHE (10 μ M, 1 h). (A) HPLC traces were recorded with the diode array detector set at 370 nm. (B) same as (A) but with changes in the peak intensities of 2-OH-TMeE⁺ as shown. (C) Quantitative data on intracellular levels of TMeHE and its oxidation products, as the amount normalized to total cellular protein. T-test vs. control: *p < 0.01.

increase the yield of the superoxide-specific product, even if the $O_2^{\bullet-}$ level *per se* is not increased. We have previously reported similar observations regarding the effect of peroxidase on the yield of 2-OH-E⁺³³.

We also estimated the second-order rate constant for the reaction of HO_2^{\bullet} with HE as $\sim 1 \times 10^7 M^{-1}s^{-1}$ (Fig. 4). Using this value and taking into account the pK_a value of HO_2^{\bullet} (4.8)⁴⁹ the apparent second-order rate constant of the reaction between $O_2^{\bullet-}$ and HE at pH 7.4 was found to be equal to $2.5 \times 10^4 M^{-1}s^{-1}$. This apparent rate constant was calculated assuming that, in the system producing $O_2^{\bullet-}$, HO_2^{\bullet} is the sole species oxidizing HE. This value is in reasonable agreement with the value determined from competition kinetics with SOD, $k = (6.2 \pm 0.8) \times 10^3 M^{-1}s^{-1}$ ¹²⁸, and is one order of magnitude higher than the value obtained from fluorescence measurements coupled to computational modeling, $k = (2.17 \pm 0.06) \times 10^3 M^{-1}s^{-1}$ ¹⁵⁰. Additionally, this value is in a good agreement with those obtained for HPr⁺ and MitoHE, $k = (1.19 \pm 0.05) \times 10^4 M^{-1}s^{-1}$ and $k = (1.6 \pm 0.8) \times 10^4 M^{-1}s^{-1}$, respectively²⁸. Taking into account that the chemical reactivities of HE, Mito-HE, and HPr⁺ are very similar, this suggests that HO_2^{\bullet} is the actual species oxidizing HE and HE derivatives in the $O_2^{\bullet-}$ producing system. Further studies are required to explore the possibility of the involvement of proton-coupled electron transfer (PCET) in the mechanism of oxidation of HE-based probes by $O_2^{\bullet-}$ ^{51,52}.

Experiments under cryogenic conditions enable unambiguous assignment of the observed transient species to the radical cations of HPr⁺ and HE, and exclude the contribution of aromatic aminyl radicals (HPr⁺ (*NH) or HE (*NH)) to the observed absorption spectra (Fig. 5). The good agreement between the experimental data obtained from cryogenic measurements for radical cations of HE, HPr⁺, MeE, and TMeHE and the results obtained from TD-DFT calculations also confirms the proper assignment of the primary species observed in the time-resolved pulse radiolytic studies (Fig. 3). Moreover, the characteristic electronic absorption spectra obtained from cryogenic measurements for the radical cations of HE and HPr⁺, as well as for MeE and TMeHE (Fig. 5), are similar to the electronic absorption spectrum obtained for the benzidine radical cation (Supplementary Fig. S8). The intense and structured transient absorption bands at 450 nm, 800 nm, and 900 nm attributed to the benzidine radical cation are in agreement with literature data^{53,54}. The pK_a of the radical cation of benzidine is 10.9, which is four units higher than that of the aniline radical cation⁵⁵. The lack of differences between the spectra of HPr^{•2+} and HE^{•+} observed at pH 10.5 and pH 7.4 suggests an even higher pK_a value for these radical cations (Fig. 3)³⁴.

According to the mechanism of 2-OH-E⁺ formation, the affinity of nucleophilic $O_2^{\bullet-}$ to the radical cation should depend strongly on the spin density at the C-2 carbon atom and to a lesser extent, due to the small size of the $O_2^{\bullet-}$ molecule, on the steric hindrance of the α -amine group. Quantum mechanical calculations showed that the highest spin density was located at the C-2 and C-12 carbon atoms of the HPr⁺, HE, MeE, and TMeHE radical cations (Supplementary Fig. S4 and Table S3). This supports the hypothesis that $O_2^{\bullet-}$ reacts with the

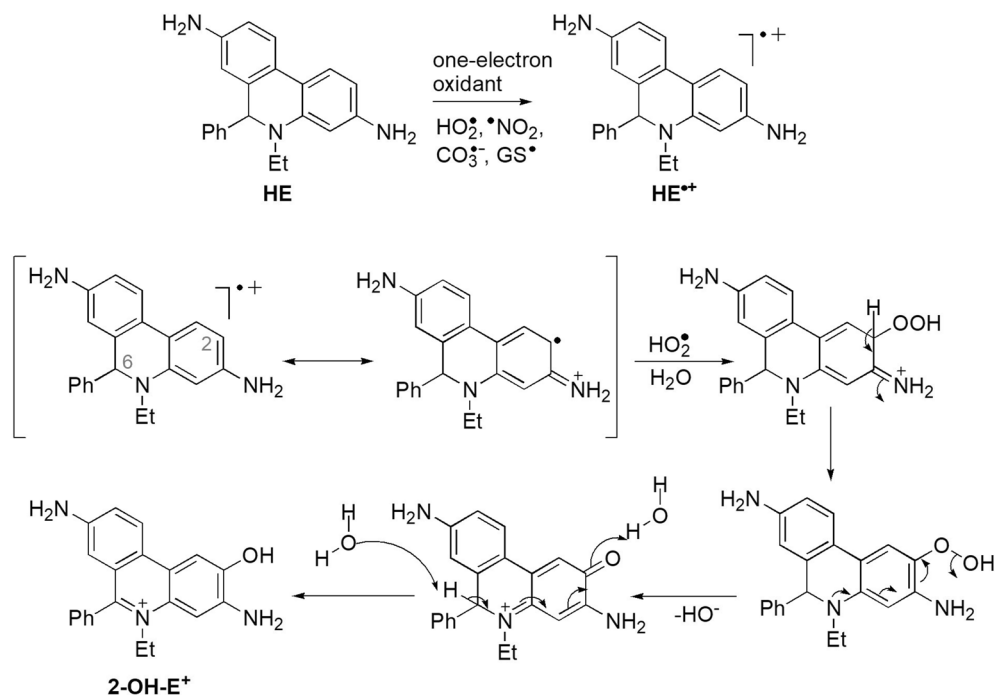


Figure 10. Mechanism of HE oxidation to 2-OH-E⁺ in the presence of one-electron oxidants and O₂^{•-}.

radical cation of the hydroethidine-based probe, through a direct attack on the C-2 carbon atom, yielding the 2-hydroxylated cationic product.

Using close structural analogues of HE, namely HPr⁺ and TMeHPr⁺, we demonstrated that the radical cations of both probes react with O₂^{•-} with high reaction rates (Fig. 7, Supplementary Figure S5 and Table S4). To our knowledge, this is the first direct observation of this reaction, and it explains the recently reported incorporation of an oxygen atom from ¹⁸O₂^{•-} in the 2-OH-E⁺ product⁵⁶.

Our results led us to postulate the following mechanism for the oxidation of HE to 2-OH-E⁺ that is relevant to its other derivatives (Fig. 10). In the first step, HE is oxidized to the radical cation by one-electron oxidants like •NO₂, CO₃^{•-}, GS[•] or HO₂[•]. Then, the recombination of HE^{•+} with O₂^{•-} forms a hydroperoxide derivative followed by elimination of hydroxide to form a quinone derivative. The final step of the reaction is the transformation of the quinone derivative to 2-OH-E⁺ (Fig. 10).

In the absence of superoxide, the radical cation of HE and its derivatives decay by dimerization and/or by disproportionation reaction (Fig. 2). Interestingly, methylation of the exocyclic amine groups blocks dimerization of the radical cation. Probably, the bulky α -dimethylamino group present in the structures of TMeHE and TMeHPr⁺ causes steric hindrance around the C-2 carbon atom, the site of new C-C bond formation by two dimerizing radicals^{28,31}, and impedes dimer formation for TMeHE and TMeHPr⁺.

We also examined the reactivity of TMeHE toward superoxide (Supplementary Fig. S7). In the presence of O₂^{•-}, TMeHE was found to form 2-OH-TMeE⁺. In combination with the fact that one-electron oxidation of TMeHE is not accompanied by the formation of any dimeric products (Supplementary Fig. S6), this finding encouraged us to test TMeHE in the cellular system. Incubation of TMeHE with cells activated to produce O₂^{•-} resulted in the formation of 2-OH-TMeE⁺ (Fig. 9). This result is in agreement with the results obtained for the HE probe reported previously^{29,30,34,57–60}. Overall, TMeHE can be utilized for the detection of cellular O₂^{•-} and, taking into account its less complicated oxidation products profile, TMeHE seems to be an improved candidate for this specific purpose. Furthermore, the unimpeded reactivity of the N-methylated analogs towards superoxide open the way for future modifications of the probes using amine groups as the site of derivatization.

Conclusions

This study has demonstrated that hydroethidine and related probes are rapidly oxidized by an array of biologically relevant oxidants, including HO[•], •NO₂, CO₃^{•-}, GS[•], and CysS[•]. The initial product of this reaction is the radical cation of the probe. Analysis of the kinetics of oxidation of HE by different peroxy radicals and by superoxide, points to HO₂[•] as the actual oxidant of HE in the presence of O₂^{•-}. We have also demonstrated that the radical cation formed during oxidation of the probe by HO₂[•] or other oxidants, reacts rapidly with O₂^{•-} to produce the O₂^{•-}-specific hydroxylated product. Methylation of the amine groups of HE was found to block the dimerization of the probe simplifying product distribution, while not significantly affecting the reaction with O₂^{•-}. This opens a new route for the derivatization of the HE probe and the generation of new analogs for improved performance in detecting O₂^{•-} in biological systems.

Methods

All synthetic procedures including the synthesis of HPr⁺, TMeHE, TMeE⁺, 2-OH-TMeE⁺, TMeHPr⁺, TMePr⁺⁺, 2-OH-TMePr⁺⁺, and MeE, together with the MS and NMR data, are described in the SI. Pulse radiolysis experiments were performed with a 6-MeV linear accelerator at the Institute of Applied Radiation Chemistry (Lodz, Poland). A detailed description of the experiments is given in the SI.

Kinetic simulations. The kinetic simulations were carried out using Kintecus 4.80⁶¹. The list of the chemical reactions and values of the corresponding rate constants are shown in SI.

Cryogenic measurements. Ionic liquid-based cryogenic glasses were prepared by immersing a solution of the appropriate compound in liquid nitrogen. The thickness of the glassy samples was below 1 mm. The samples were placed in a temperature-controlled, liquid nitrogen-cooled cryostat (OptiStat DN, Oxford Instruments, United Kingdom), then irradiated with 4 μs electron pulses from a linear accelerator. The UV-Vis absorption spectra were recorded with a Cary 5 (Varian Medical Systems, United States) spectrophotometer. Radiolysis of the glassy sample of BMIM⁺PF₆⁻ results in the generation of electrons and oxidizing holes represented by the 1-butyl-3-methylimidazolium (BMIM^{•2+}) radical dication and hexafluorophosphate radical (PF₆[•]). Solvated electrons are captured by BMIM⁺ cations yielding BMIM[•] radicals, which prevent geminate recombination of the primary species^{62,63}. In the presence of halogenated compounds like dichloromethane, instead of BMIM[•] formation, the electrons are scavenged through dissociative electron attachment^{64,65}. BMIM^{•2+} and PF₆[•] are strong one-electron oxidants; they accept electrons from the solute molecules of lower ionization potential (e.g., HPr⁺) producing the corresponding one-electron oxidized species (e.g., HPr^{•2+}).

QM calculations. All calculations were performed using the Gaussian G09W suite of programs⁶⁶. The gas-phase geometry of the studied radical cations was optimized using the unrestricted B3LYP density functional method^{67,68}. The 6-311+G(d,p) basis set was used for geometry optimizations and energy calculations. No imaginary frequencies were observed for the converged structures of the studied radical cations. Mulliken atomic spin densities were obtained from the gas-phase UB3LYP/6-31+G(d, p) geometries. Spin density maps were generated from formatted checkpoints using the Cubegen utility provided with Gaussian. Spin density maps were formed by the superposition of the spin density surface on the electron density surface. Excited-state calculations were carried out on the basis of time-dependent response theory, along with unrestricted B3LYP density functional theory (the so-called time-dependent density functional theory [TD-DFT] method)⁶⁹. All calculations were carried out with the default convergence criteria.

UPLC/UV-Vis/MS analyses. The ultra-performance liquid chromatography (UPLC) system (UPLC Acquity, Waters Ltd., United States) equipped with a photodiode array detector for UV-Vis absorption measurements and LCT Premier XE (Water Micromass, United States) mass spectrometry detector was used to investigate the products of the reaction of TMeHE and TMeHPr⁺ with the oxidants. Separation of TMeHE was accomplished on a Waters Ltd. UPLC column (Acquity UPLC BEH C18, 1.7 μm, 50 × 2.1 mm), kept at 40 °C and equilibrated with a mobile phase consisting of water/MeCN, 70:30 (v/v), at a flow rate of 0.3 ml/min for at least 0.5 min. Both the organic and water phases contained 0.1% (v/v) trifluoroacetic acid (TFA). Next, the concentration of organic phase was increased linearly up to 70% (v/v) over 1.55 min. It was then raised rapidly up to 100% (v/v) over the next 0.1 min and kept at this level for 0.65 min. The analytes, TMeHE, 2-OH-TMeE⁺, and TMeE⁺, were eluted at retention times of 1.53 min, 1.72 min, and 2.44 min, respectively, and detected by monitoring the absorption at 370 ± 10 nm.

Separation of TMeHPr⁺ was performed using an Acquity UPLC CSH Phenyl-Hexyl column (1.7 μm, 50 × 2.1 mm) equilibrated with water/methanol mobile phase (60:40 v/v) containing 0.1% vol. of TFA, at a flow rate of 0.3 ml/min. The TMeHPr⁺, 2-OH-TMePr⁺⁺, and TMePr⁺⁺ were eluted at retention times of 0.83 min, 0.97 min, and 1.46 min, respectively, using the following gradient method: The initial concentration of the organic phase was applied for 0.5 min; over next 1.5 min concentration of organic phase was increased linearly to 100%; the column was then rinsed with 100% (v/v) organic phase for another 1 min.

The products of HE oxidation by ferricyanide anion were separated using an Acquity UPLC BEH C18 column (1.7 μm, 50 × 2.1 mm) and the gradient method, as described elsewhere³². The identity of the analytes was confirmed by mass spectrometry analysis using the m/z ratio obtained from the experiment and calculated based on the molecular structure, as shown in Supplementary Tables S1 and S2. The injection volumes and temperatures for both the samples and the standard solutions were 2 μl and 23 °C in case of the TMeHE and HE probes, and 0.5 μl and 20 °C for TMeHPr⁺. Data acquisition was performed using MassLynx 4.1 data software (Waters Ltd., United States).

Cell culture experiments. RAW 264.7 cells were obtained over the last five years, stored in liquid nitrogen, and used within 20 passages after thawing. The cells were grown at 37 °C in 5% CO₂. The cells were maintained in DMEM (CAT#11965, Invitrogen, San Diego, CA) containing 10% (v/v) fetal bovine serum, penicillin (100 U/ml) and streptomycin (0.1 mg/ml).

The RAW 264.7 cells were cultured as described previously²⁸. The cells were incubated with phorbol 12-myristate 13-acetate (PMA, 1 μM) and TMeHE (10 μM) for 1 hour at 37 °C in 5% CO₂. After incubation, 100 μL of the medium was transferred to an Eppendorf tube and frozen in liquid nitrogen. The rest of the medium was discarded and the cells were washed twice using ice-cold Dulbecco's phosphate buffered saline (DPBS). The

washed cells were scraped in 1 mL of DPBS, transferred to an Eppendorf tube and centrifuged for 1 min. Then, the supernatant was aspirated and the cell pellet was frozen in liquid nitrogen.

Processing of cell pellets. Frozen cell pellets were placed on ice and syringe lysed, using 10 strokes through a 28 ga needle, in 200 μ l of 0.1% vol. Triton X-100 in ice-cold phosphate buffered saline containing 1 μ M of 3,8-diamino-6-phenylphenanthridine (DAPP) as an internal standard. The probes and their oxidation products were then extracted by adding 100 μ l of the resulting mixture to 100 μ l of 0.1% vol. formic acid in MeCN. The samples were incubated on ice for 1 h, and then centrifuged for 30 min at 20,000g at 4 °C. A volume of 100 μ L of the supernatant was then transferred to a fresh tube containing 100 μ l of 0.1% vol. formic acid in water. This solution was centrifuged for an additional 15 min at 20,000g at 4 °C. A volume of 150 μ L of the resulting supernatant was then transferred to HPLC vials for analysis⁵⁹.

HPLC analysis of cell extracts. HPLC analyses were performed by adopting the previous method⁷⁰. The samples were separated using an Agilent 1100 system (North Billerica, MA) equipped with absorption and fluorescence detectors. During the HPLC analyses, samples were stored at 4 °C and the injection volume was 50 μ l. For the separation of analytes, a reverse phase column (Phenomenex, Kinetex C18, 100 mm \times 4.6 mm, 2.6 μ m) was used. Prior to injection, the column was equilibrated with a mobile phase consisting of 20% MeCN and 80% water (v/v). The organic and aqueous mobile phases contained 0.1% (v/v) TFA.

The TMeHE and its oxidation products were separated using the gradient method. The fraction of MeCN was increased during the analysis linearly from 20 to 40% over 1 min, then, from 40 to 49% over 2 min and from 49 to 100% over 2 min. An absorption detector was used to measure DAPP (at 290 nm; retention time: 2.0 min), 2-OH-TMeE⁺ (at 290 nm; retention time: 2.9 min), and TMeHE (at 370 nm; retention time: 2.4 min). TMeHE, 2-OH-TMeE⁺, and TMeE⁺ were also monitored fluorometrically using the following excitation and emission wavelengths: 358 nm/400 nm for TMeHE, 490 nm/608 nm for 2-OH-TMeE⁺, and 555 nm/625 nm for TMeE⁺ (retention time: 4.8 min).

Received: 15 May 2020; Accepted: 13 October 2020

Published online: 29 October 2020

References

- Bedard, K. & Krause, K. H. The nox family of ros-generating nadph oxidases: Physiology and pathophysiology. *Physiol. Rev.* **87**, 245–313. <https://doi.org/10.1152/physrev.00044.2005> (2007).
- Fridovich, I. Quantitative aspects of the production of superoxide anion radical by milk xanthine oxidase. *J. Biol. Chem.* **245**, 4053–4057 (1970).
- Murphy, M. P. How mitochondria produce reactive oxygen species. *Biochem. J.* **417**, 1–13. <https://doi.org/10.1042/Bj20081386> (2009).
- Augusto, O. *et al.* Carbon dioxide-catalyzed peroxynitrite reactivity - the resilience of the radical mechanism after two decades of research. *Free Radic Biol Med* **135**, 210–215. <https://doi.org/10.1016/j.freeradbiomed.2019.02.026> (2019).
- Beckman, J. S., Beckman, T. W., Chen, J., Marshall, P. A. & Freeman, B. A. Apparent hydroxyl radical production by peroxynitrite: Implications for endothelial injury from nitric oxide and superoxide. *Proc. Natl. Acad. Sci. USA* **87**, 1620–1624. <https://doi.org/10.1073/pnas.87.4.1620> (1990).
- Chance, B., Sies, H. & Boveris, A. Hydroperoxide metabolism in mammalian organs. *Physiol. Rev.* **59**, 527–605. <https://doi.org/10.1152/physrev.1979.59.3.527> (1979).
- Zielonka, J., Sikora, A., Joseph, J. & Kalyanaraman, B. Peroxynitrite is the major species formed from different flux ratios of co-generated nitric oxide and superoxide: Direct reaction with boronate-based fluorescent probe. *J. Biol. Chem.* **285**, 14210–14216. <https://doi.org/10.1074/jbc.M110.110080> (2010).
- Sies, H. Oxidative stress: A concept in redox biology and medicine. *Redox. Biol.* **4**, 180–183. <https://doi.org/10.1016/j.redox.2015.01.002> (2015).
- Reuter, S., Gupta, S. C., Chaturvedi, M. M. & Aggarwal, B. B. Oxidative stress, inflammation, and cancer: How are they linked?. *Free Radic. Biol. Med.* **49**, 1603–1616. <https://doi.org/10.1016/j.freeradbiomed.2010.09.006> (2010).
- Sugamura, K. & Keane, J. F. Jr. Reactive oxygen species in cardiovascular disease. *Free Radic. Biol. Med.* **51**, 978–992. <https://doi.org/10.1016/j.freeradbiomed.2011.05.004> (2011).
- Sohal, R. S. & Orr, W. C. The redox stress hypothesis of aging. *Free Radic. Biol. Med.* **52**, 539–555. <https://doi.org/10.1016/j.freeradbiomed.2011.10.445> (2012).
- Wardman, P. Fluorescent and luminescent probes for measurement of oxidative and nitrosative species in cells and tissues: Progress, pitfalls, and prospects. *Free Radic. Biol. Med.* **43**, 995–1022. <https://doi.org/10.1016/j.freeradbiomed.2007.06.026> (2007).
- Gao, X. Y. *et al.* A two-channel responsive fluorescent probe with aie characteristics and its application for selective imaging of superoxide anions in living cells. *Chem. Commun.* **53**, 1653–1656. <https://doi.org/10.1039/c6cc09307h> (2017).
- Hong, S. C. *et al.* Discrimination of avian influenza virus subtypes using host-cell infection fingerprinting by a sulfinate-based fluorescence superoxide probe. *Angewandte Chem. Int. Edition* **57**, 9716–9721. <https://doi.org/10.1002/anie.201804412> (2018).
- Li, P. *et al.* Mitochondria-targeted reaction-based two-photon fluorescent probe for imaging of superoxide anion in live cells and in vivo. *Anal. Chem.* **85**, 9877–9881. <https://doi.org/10.1021/ac402409m> (2013).
- Maeda, H. *et al.* A design of fluorescent probes for superoxide based on a nonredox mechanism. *J. Am. Chem. Soc.* **127**, 68–69. <https://doi.org/10.1021/ja047018k> (2005).
- Manjare, S. T., Kim, S., Heo, W. D. & Churchill, D. G. Selective and sensitive superoxide detection with a new diselenide-based molecular probe in living breast cancer cells. *Organ. Lett.* **16**, 410–412. <https://doi.org/10.1021/ol4033013> (2014).
- Yu, Z. H., Chung, C. Y. S., Tang, F. K., Brewer, T. F. & Au-Yeung, H. Y. A modular trigger for the development of selective superoxide probes. *Chem. Commun.* **53**, 10042–10045. <https://doi.org/10.1039/c7cc05405j> (2017).
- Zhang, J. J. *et al.* A phosphinate-based near-infrared fluorescence probe for imaging the superoxide radical anion in vitro and in vivo. *Chem. Commun.* **52**, 2679–2682. <https://doi.org/10.1039/c5cc09976e> (2016).
- Zhang, W. *et al.* Dynamic and reversible fluorescence imaging of superoxide anion fluctuations in live cells and in vivo. *J. Am. Chem. Soc.* **135**, 14956–14959. <https://doi.org/10.1021/ja408524j> (2013).

21. Fink, B. *et al.* Detection of intracellular superoxide formation in endothelial cells and intact tissues using dihydroethidium and an hplc-based assay. *Am. J. Physiol. Cell Physiol.* **287**, C895–C902. <https://doi.org/10.1152/ajpcell.00028.2004> (2004).
22. Georgiou, C. D., Papapostolou, I., Patsoukis, N., Tseggenidis, T. & Sideris, T. An ultrasensitive fluorescent assay for the in vivo quantification of superoxide radical in organisms. *Anal. Biochem.* **347**, 144–151. <https://doi.org/10.1016/j.ab.2005.09.013> (2005).
23. Proniewski, B., Kij, A., Sitek, B., Kelley, E. E. & Chlopicki, S. Multiorgan development of oxidative and nitrosative stress in lps-induced endotoxemia in c57bl/6 mice: Dhe-based in vivo approach. *Oxidative Medicine and Cellular Longevity* <https://doi.org/10.1155/2019/7838406> (2019).
24. Robinson, K. M. *et al.* Selective fluorescent imaging of superoxide in vivo using ethidium-based probes. *Proc. Natl. Acad. Sci. USA* **103**, 15038–15043. <https://doi.org/10.1073/pnas.0601945103> (2006).
25. Seredenina, T. *et al.* Evaluation of nadph oxidases as drug targets in a mouse model of familial amyotrophic lateral sclerosis. *Free Rad. Biol. Med.* **97**, 95–108. <https://doi.org/10.1016/j.freeradbiomed.2016.05.016> (2016).
26. Zielonka, J. & Kalyanaraman, B. Small-molecule luminescent probes for the detection of cellular oxidizing and nitrating species. *Free Radic. Biol. Med.* **128**, 3–22. <https://doi.org/10.1016/j.freeradbiomed.2018.03.032> (2018).
27. Shchepinova, M. M. *et al.* Mitoneod: A mitochondria-targeted superoxide probe. *Cell Chem. Biol.* **24**, 1285–1298. <https://doi.org/10.1016/j.chembiol.2017.08.003> (2017).
28. Michalski, R., Zielonka, J., Hardy, M., Joseph, J. & Kalyanaraman, B. Hydropropidine: a novel, cell-impermeant fluorogenic probe for detecting extracellular superoxide. *Free Radic. Biol. Med.* **54**, 135–147. <https://doi.org/10.1016/j.freeradbiomed.2012.09.018> (2013).
29. Zielonka, J. *et al.* High-throughput assays for superoxide and hydrogen peroxide: Design of a screening workflow to identify inhibitors of nadph oxidases. *J. Biol. Chem.* **289**, 16176–16189. <https://doi.org/10.1074/jbc.M114.548693> (2014).
30. Zielonka, J. *et al.* Mitigation of nadph oxidase 2 activity as a strategy to inhibit peroxynitrite formation. *J. Biol. Chem.* **291**, 7029–7044. <https://doi.org/10.1074/jbc.M115.702787> (2016).
31. Zielonka, J. *et al.* Cytochrome c-mediated oxidation of hydroethidine and mito-hydroethidine in mitochondria: Identification of homo- and heterodimers. *Free Radic. Biol. Med.* **44**, 835–846. <https://doi.org/10.1016/j.freeradbiomed.2007.11.013> (2008).
32. Koto, T., Michalski, R., Zielonka, J., Joseph, J. & Kalyanaraman, B. Detection and identification of oxidants formed during $\text{no}^{\cdot-}/\text{o}_2^{\cdot-}$ reaction: A multi-well plate cw-epr spectroscopy combined with hplc analyses. *Free Radic. Res.* **48**, 478–486. <https://doi.org/10.3109/10715762.2014.886774> (2014).
33. Michalski, R., Michalowski, B., Sikora, A., Zielonka, J. & Kalyanaraman, B. On the use of fluorescence lifetime imaging and dihydroethidium to detect superoxide in intact animals and ex vivo tissues: A reassessment. *Free Radic. Biol. Med.* **67**, 278–284. <https://doi.org/10.1016/j.freeradbiomed.2013.10.816> (2014).
34. Zielonka, J., Hardy, M. & Kalyanaraman, B. Hplc study of oxidation products of hydroethidine in chemical and biological systems: Ramifications in superoxide measurements. *Free Radic. Biol. Med.* **46**, 329–338. <https://doi.org/10.1016/j.freeradbiomed.2008.10.031> (2009).
35. Zielonka, J., Sarna, T., Roberts, J. E., Wishart, J. F. & Kalyanaraman, B. Pulse radiolysis and steady-state analyses of the reaction between hydroethidine and superoxide and other oxidants. *Arch. Biochem. Biophys.* **456**, 39–47. <https://doi.org/10.1016/j.abb.2006.09.031> (2006).
36. Zielonka, J., Vasquez-Vivar, J. & Kalyanaraman, B. Detection of 2-hydroxyethidium in cellular systems: A unique marker product of superoxide and hydroethidine. *Nat. Protoc.* **3**, 8–21. <https://doi.org/10.1038/nprot.2007.473> (2008).
37. Zielonka, J., Zhao, H., Xu, Y. & Kalyanaraman, B. Mechanistic similarities between oxidation of hydroethidine by fremy's salt and superoxide: Stopped-flow optical and epr studies. *Free Radic. Biol. Med.* **39**, 853–863. <https://doi.org/10.1016/j.freeradbiomed.2005.05.001> (2005).
38. Zielonka, J. & Kalyanaraman, B. Hydroethidine- and mitoxo-derived red fluorescence is not a reliable indicator of intracellular superoxide formation: Another inconvenient truth. *Free Radic. Biol. Med.* **48**, 983–1001. <https://doi.org/10.1016/j.freeradbiomed.2010.01.028> (2010).
39. Kalyanaraman, B., Dranka, B. P., Hardy, M., Michalski, R. & Zielonka, J. Hplc-based monitoring of products formed from hydroethidine-based fluorogenic probes—the ultimate approach for intra- and extracellular superoxide detection. *Biochim. Biophys. Acta* **739–744**, 2014. <https://doi.org/10.1016/j.bbagen.2013.05.008> (1840).
40. Behar, D., Czapski, G. & Duchovny, I. Carbonate radical in flash photolysis and pulse radiolysis of aqueous carbonate solutions. *J. Phys. Chem.* **74**, 2206–2210. <https://doi.org/10.1021/j100909a029> (1970).
41. Mozziconacci, O., Williams, T. D. & Schöneich, C. Intramolecular hydrogen transfer reactions of thiyl radicals from glutathione: Formation of carbon-centered radical at glu, cys, and gly. *Chem. Res. Toxicol.* **25**, 1842–1861. <https://doi.org/10.1021/tx3000494> (2012).
42. Hofstetter, D., Nauser, T. & Koppenol, W. H. Hydrogen exchange equilibria in glutathione radicals: Rate constants. *Chem. Res. Toxicol.* **23**, 1596–1600. <https://doi.org/10.1021/tx3000494> (2010).
43. Jacquemin, D., Wathelet, V., Perpete, E. A. & Adamo, C. Extensive td-dft benchmark: Singlet-excited states of organic molecules. *J. Chem. Theory Comput.* **5**, 2420–2435. <https://doi.org/10.1021/ct900298e> (2009).
44. Miralles, A. J., Armstrong, R. E. & Haim, A. Outer-sphere reductions of pyridinepentaamminecobalt(iii) and pyridinepentaammineiruthenium(iii) by hexacyanoferrate(ii). *J. Am. Chem. Soc.* **99**, 1416–1420. <https://doi.org/10.1021/ja00447a022> (1977).
45. Koppenol, W. H., Serrano-Luginbuehl, S., Nauser, T. & Kissner, R. Thinking outside the cage: A new hypothesis that accounts for variable yields of radicals from the reaction of co_2 with $\text{onoo}^{\cdot-}$. *Chem. Res. Toxicol. In Press* <https://doi.org/10.1021/acs.chemrestox.9b00309> (2020).
46. Mahmoudi, L., Kissner, R., Nauser, T. & Koppenol, W. H. Electrode potentials of l-tryptophan, l-tyrosine, 3 nitro-l-tyrosine, 2,3-diuro-l-tyrosine, and 2,3,5-triuoro-l-tyrosine. *Biochemistry* **55**, 2849–2856. <https://doi.org/10.1021/acs.biochem.6b00019> (2016).
47. Prütz, W. A., Butler, J., Land, E. J. & Swallow, A. J. Direct demonstration of electron-transfer between tryptophan and tyrosine in proteins. *Biochem. Biophys. Res. Commun.* **96**, 408–414. [https://doi.org/10.1016/0006-291X\(80\)91230-9](https://doi.org/10.1016/0006-291X(80)91230-9) (1980).
48. Petruk, A. A. *et al.* Molecular basis of intramolecular electron transfer in proteins during radical-mediated oxidations: Computer simulation studies in model tyrosine-cysteine peptides in solution. *Arch. Biochem. Biophys.* **525**, 82–91. <https://doi.org/10.1016/j.abb.2012.05.012> (2012).
49. Armstrong, D. A. *et al.* Standard electrode potentials involving radicals in aqueous solution: Inorganic radicals (iupac technical report). *Pure Appl. Chem.* **87**, 1139–1150. <https://doi.org/10.1515/pac-2014-0502> (2015).
50. Chen, J., Rogers, S. C. & Kavdia, M. Analysis of kinetics of dihydroethidium fluorescence with superoxide using xanthine oxidase and hypoxanthine assay. *Ann. Biomed. Eng.* **41**, 327–337. <https://doi.org/10.1007/s10439-012-0653-x> (2013).
51. Sawyer, D. T. & Valentine, J. S. How super is superoxide?. *Accounts of Chemical Research* **14**, 393–400. <https://pubs.acs.org/doi/10.1021/ar00072a005> (1981).
52. Hayyan, M., Hashim, M. A. & AlNashef, I. M. Superoxide ion: Generation and chemical implications. *Chem. Rev.* **116**, 3029–3085. <https://doi.org/10.1021/acs.chemrev.5b00407> (2016).
53. Jacob, J. A., Naumov, S., Biswas, N., Mukherjee, T. & Kapoor, S. Comparative study of ionization of benzidine and its derivatives by free electron transfer and one-electron oxidation. *J. Phys. Chem. C* **111**, 18397–18404. <https://doi.org/10.1021/jp075585z> (2007).
54. Chen, X. *et al.* From monomers to π stacks, from nonconductive to conductive: Syntheses, characterization, and crystal structures of benzidine radical cations. *Chemistry* **18**, 11828–11836. <https://doi.org/10.1002/chem.201103972> (2012).

55. Tripathi, G. N. R. & Schuler, R. H. Time resolved absorption and resonance raman spectroscopic studies of the oxidation of benzidine in aqueous solution. *Int J Radiat Appl Instrum Part C. Radiat. Phys. Chem.* **32**, 251–258. [https://doi.org/10.1016/1359-0197\(88\)90194-4](https://doi.org/10.1016/1359-0197(88)90194-4) (1988).
56. Rios, N., Radi, R., Kalyanaraman, B. & Zielonka, J. Tracking isotopically labeled oxidants using boronate-based redox probes. *J. Biol. Chem.* **295**, 6665–6676. <https://doi.org/10.1074/jbc.RA120.013402> (2020).
57. Hardy, M. *et al.* Detection and characterization of reactive oxygen and nitrogen species in biological systems by monitoring species-specific products. *Antioxid. Redox. Sign.* **28**, 1416–1432. <https://doi.org/10.1089/ars.2017.7398> (2018).
58. Zielonka, J. *et al.* Recent developments in the probes and assays for measurement of the activity of nadph oxidases. *Cell. Biochem. Biophys.* **75**, 335–349. <https://doi.org/10.1007/s12013-017-0813-6> (2017).
59. Zielonka, J., Zielonka, M. & Kalyanaraman, B. Hplc-based monitoring of oxidation of hydroethidine for the detection of nadph oxidase-derived superoxide radical anion. *Nadph Oxidases Methods Protocols* **243–258**, 2019. https://doi.org/10.1007/978-1-4939-9424-3_14 (1982).
60. Zielonka, J. *et al.* Global profiling of reactive oxygen and nitrogen species in biological systems: High-throughput real-time analyses. *J. Biol. Chem.* **287**, 2984–2995. <https://doi.org/10.1074/jbc.M111.309062> (2012).
61. Ianni, J. C. Windows version 6.8. www.kintecus.com (2019).
62. Marcinek, A., Zielonka, J., Gebicki, J., Gordon, C. M. & Dunkin, I. R. Ionic liquids: Novel media for characterization of radical ions. *J. Phys. Chem. A* **105**, 9305–9309. <https://doi.org/10.1021/jp0117718> (2001).
63. Behar, D., Gonzales, C. & Neta, P. Reaction kinetics in ionic liquids: Pulse radiolysis studies of 1-butyl-3-methylimidazolium salts. *J. Phys. Chem. A* **105**, 7607–7614. <https://doi.org/10.1021/jp011405o> (2001).
64. Czzerwinska, M. *et al.* Anthralin: Primary products of its redox reactions. *J. Organ. Chem.* **71**, 5312–5319. <https://doi.org/10.1021/jo060622o> (2006).
65. Michalski, R., Sikora, A., Adamus, J. & Marcinek, A. Mechanistic aspects of radiation-induced oligomerization of 3,4-ethylenedioxythiophene in ionic liquids. *J. Phys. Chem. A* **114**, 11552–11559. <https://doi.org/10.1021/jp1067389> (2010).
66. Frisch, M. *et al.* Gaussian 09, revision a. 02. gaussian, Inc., Wallingford, CT (2009).
67. Becke, A. D. Density-functional thermochemistry. ii. the effect of the perdew-wang generalized-gradient correlation correction. *J. Chem. Phys.* **97**, 9173–9177. <https://doi.org/10.1063/1.463343> (1992).
68. Lee, C., Yang, W. & Parr, R. G. Development of the colle-salvetti correlation-energy formula into a functional of the electron density. *Phys. Rev. B Condens. Matter* **37**, 785–789. <https://doi.org/10.1103/PhysRevB.37.785> (1988).
69. Casida, M. E. Time-dependent density-functional theory for molecules and molecular solids. *J. Mol. Struct. Theochem* **914**, 3–18. <https://doi.org/10.1016/j.theochem.2009.08.018> (2009).
70. Cheng, G. *et al.* Detection of mitochondria-generated reactive oxygen species in cells using multiple probes and methods: Potentials, pitfalls, and the future. *J. Biol. Chem.* **293**, 10363–10380. <https://doi.org/10.1074/jbc.RA118.003044> (2018).
71. Das, T. N., Dhanasekaran, T., Alfassi, Z. B. & Neta, P. Reduction potential of the tert-butylperoxyl radical in aqueous solutions. *J. Phys. Chem. A* **102**, 280–284. <https://doi.org/10.1021/jp972903t> (1998).

Acknowledgements

This study was supported by a grant from the Foundation for Polish Science (FNP) within the “Homing Plus” program (Homing Plus 2010/1/12) supported by the European Union within European Regional Development Fund, through the Innovative Economy Programme, and by a grant from the Polish National Science Centre (NCN) within the SONATA BIS 5 program (Grant No. 2015/18/E/ST4/00235). J.Z. was supported in part by an Institutional Research Grant IRG #16-183-31 from the American Cancer Society and the MCW Cancer Center. R.M. was supported by the Polish National Science Centre (NCN) within the SONATA program (Grant No. 2018/31/D/ST4/03494). This work was also supported by the PACA region (Apex, Fluo2) and ANR (ANR-16-CE07-0023-01 (Vivo2)).

Author contributions

R.M., B.M., and A.A. performed pulse radiolysis experiments. D.T., M.H., O.O., and M.M.A. were involved in syntheses. D.T. and J.Z. performed the experiments on cells. B.M. and M.R. performed all quantum-mechanical calculations. R.M. performed chromatographic experiments. R.M., B.M., and A.S. performed analysis and interpretation of data. R.S.I., A.M., J.Z., O.O., and B.K. revised the paper critically for important intellectual content. R.M. and A.S. conceived the main idea. All authors were involved in preparation of the manuscript.

Competing interests

The authors declare no competing interests.

Additional information

Supplementary information is available for this paper at <https://doi.org/10.1038/s41598-020-75373-2>.

Correspondence and requests for materials should be addressed to R.M. or A.S.

Reprints and permissions information is available at www.nature.com/reprints.

Publisher’s note Springer Nature remains neutral with regard to jurisdictional claims in published maps and institutional affiliations.



Open Access This article is licensed under a Creative Commons Attribution 4.0 International License, which permits use, sharing, adaptation, distribution and reproduction in any medium or format, as long as you give appropriate credit to the original author(s) and the source, provide a link to the Creative Commons licence, and indicate if changes were made. The images or other third party material in this article are included in the article’s Creative Commons licence, unless indicated otherwise in a credit line to the material. If material is not included in the article’s Creative Commons licence and your intended use is not permitted by statutory regulation or exceeds the permitted use, you will need to obtain permission directly from the copyright holder. To view a copy of this licence, visit <http://creativecommons.org/licenses/by/4.0/>.

© The Author(s) 2020